

DOI: 10.1002/((please add manuscript number))

Article type: Communication

Elucidation of the Synergistic Effect of Dopants and Vacancies on Promoted Selectivity for CO₂ Electroreduction to Formate

Zhongjian Li, Ang Cao, Qiang Zheng, Yuanyuan Fu, Tingting Wang, K. Thanigal Arul, Jeng-Lung Chen, Bin Yang, Nadia Mohd Adli, Lecheng Lei, Chung-Li Dong, Jianping Xiao, Gang Wu,* Yang Hou**

Prof. Z. Li, Y. Fu, T. Wang, Prof. B. Yang, Prof. L. Lei, Prof. Y. Hou
College of Chemical and Biological Engineering, Zhejiang University, Hangzhou 310027, China
E-mail: yhou@zju.edu.cn (Prof. Y. Hou)

A. Cao, Prof. J. Xiao
State Key Laboratory of Catalysis, Dalian Institute of Chemical Physics, Chinese Academy of Sciences, Dalian 116023, China
E-mail: xiao@dicp.ac.cn (Prof. J. Xiao)

Prof. Q. Zheng
Key Laboratory of Standardization and Measurement for Nanotechnology, CAS Center for Excellence in Nanoscience, National Center for Nanoscience and Technology, Beijing 100190, China

K. T. Arul, Prof. C. Dong
Department of Physics, Tamkang University, New Taipei City 25137, Taiwan

Prof. J. Chen
National Synchrotron Radiation Research Center, Hsinchu 30076, Taiwan

N. Adli, Prof. G. Wu
Department of Chemical and Biological Engineering, University at Buffalo, the State University of New York, Buffalo, NY, 14260, United States
E-mail: gangwu@buffalo.edu (Prof. G. Wu)

Prof. Z. Li, Prof. B. Yang, Prof. L. Lei, Prof. Y. Hou
Institute of Zhejiang University - Quzhou, Quzhou 324000, China

Keywords: Dopants; Vacancies; CO₂ electroreduction; Formate; Zn-CO₂ battery

Abstract: Sn-based materials have been identified as promising catalysts for the CO₂ electroreduction (CO₂RR) to formate (HCOO⁻). However, their insufficient selectivity and activity remain grand challenges. We reported a new type of SnO₂ nanosheet with simultaneous N dopants and oxygen vacancies (*V_O*-rich N-SnO₂ NS) for promoting CO₂ conversion to HCOO⁻. The optimal *V_O*-rich N-SnO₂ NS possessed a unique layered structure with a thickness of ~10 nm and a high N-doping level of 5 at.%. Due to the likely synergistic effect of N dopant and *V_O*, the *V_O*-rich N-SnO₂ NS exhibited high catalytic selectivity featured by an HCOO⁻ Faradaic efficiency (FE) of 83% at -0.9 V and an FE of > 90% for all C1 products (HCOO⁻ and CO) at a wide potential range from -0.9 to -1.2 V. Experimental results revealed that low coordination Sn-N moieties are the active sites with optimal electronic and geometric structures regulated by *V_O* and N dopants, which are primarily responsible for the improved CO₂RR activity and selectivity. Theoretical calculations elucidate that the reaction free energy of HCOO* protonation is decreased on the *V_O*-rich N-SnO₂ NS, thus enhancing HCOO⁻ selectivity. The weakened H* adsorption energy also inhibited the hydrogen evolution reaction, a dominant side reaction during the CO₂RR. Furthermore, a Zn-CO₂ battery cell and a CO₂RR-oxygen evolution reaction (OER) electrolyzer were designed using the *V_O*-rich N-SnO₂ NS catalyst as the cathode. Both the spontaneous Galvanic cell and solar-powered electrolysis process successfully demonstrated the efficient HCOO⁻ generation through CO₂ conversion and storage.

Electrochemical reduction of CO₂ (CO₂RR) to value-added chemicals or fuels is a promising prospect addressing environmental and energy sustainability.^[1] Among various reduced products, formate (HCOO⁻) is desirable due to its feasibility for storage and transport, high volumetric hydrogen density, and economic profit.^[2] Recently, a variety of catalysts, such as metal oxides (Co₃O₄,^[3] SnO₂^[4]), sulfides (In₂S₃,^[5] CuS_x^[6]), and doped nanocarbon (PEI-NCNT,^[7] B-doped graphene^[8]), have been widely studied for converting CO₂ to HCOO⁻. In particular, tin oxide (SnO_x) based materials have attracted significant attention due to their encouraging formate

selectivity, low-cost, and nontoxicity.^[4,9] However, they still suffer from slow reaction dynamics and high overpotential, which needs to be addressed for viable applications.^[10]

Over the past decades, various strategies have been developed to modify SnO_x for enhancing CO₂RR performance, including morphology controlling and surface engineering.^[11] Among surface engineering, the effects of dopants and oxygen vacancies (V_O) have been extensively studied, which can efficiently tune the chemical composition and electronic structure of active sites and improve reaction kinetics.^[12,13] However, the lack is a fundamental understanding of the possible synergistic effects from dopants and V_O .^[14]

Herein, we developed a combined hydrothermal and ammonification reaction strategy to synthesize N-doped SnO₂ nanosheets with enriched V_O (denoted as V_O -rich N-SnO₂ NS). The prepared V_O -rich N-SnO₂ NS possessed a unique layered structure with a thickness of ~10 nm and a high N-doping level of 5 at.%. Due to the synergistic effect of N dopants and V_O , the V_O -rich N-SnO₂ NS exhibited an exceptional HCOO⁻ Faradaic efficiency (F.E.) of 83% at -0.9 V. The C1 products selectivity of >90% was obtained at a broad potential range from -0.9 to -1.2 V. The V_O -rich N-SnO₂ NS was one of the best SnO_x-based catalysts for the CO₂RR when compared to those reported in the literature. The possible active sites are Sn-N moieties with low coordination, evidenced by high-angle annular dark-field scanning transmission electron microscopy (HAADF-STEM) and X-ray absorption spectroscopy (XAS). Density functional theory (DFT) calculations revealed that V_O and N dopants' synergistic effect is primarily responsible for the enhanced CO₂RR activity. The reaction free energy of HCOO* protonation becomes more favorable, resulting in enhanced HCOO⁻ selectivity. Moreover, the weakened H* adsorption energy would suppress the hydrogen evolution reaction (HER). Instead of designing a CO₂RR electrolyzer, we designed and fabricated a rechargeable Zn-CO₂ battery cell for efficient CO₂ reduction to HCOO⁻ by using the V_O -rich N-SnO₂ NS catalyst as the cathode and a zinc plate as the anode. Meanwhile, as a power source, a peak power density of 3.67 mW cm⁻² can be generated from the Zn-CO₂ cell.

The synthetic procedure of the V_O -rich N-SnO₂ NS is illustrated in **Figure 1a**. A

hydrothermal reaction by using ethylenediamine was developed to prepare pristine SnO_x NS. Subsequent annealing treatment for the as-prepared SnO_x NS at a temperature of 550 °C under flowing ammonia can further introduce N dopants and oxygen vacancies. Field-emission scanning electron microscopy (FESEM) and transmission electron microscopy (TEM) analysis indicated the V_O -rich N- SnO_2 NS sample (Figures S1-S2) possesses nanosheet morphology with porous structure (**Figure 1b**) because of different diffusion rates of N and O atoms during the ammonification process.^[15] Atomic force microscopy (AFM) image and height profile determined the thickness of ~10 nm for the V_O -rich N- SnO_2 NS (Figure S3). The selected area electron diffraction pattern (SAED) (inset of **Figure 1c**) demonstrated a well-defined crystallinity of the V_O -rich N- SnO_2 NS. High-resolution TEM (HRTEM) images (**Figure 1c**) of the V_O -rich N- SnO_2 NS displayed a lattice spacing of 0.33 nm, attributable to SnO_2 (110) plane (JCPDS No. 41-1445). The circles in the images highlight the formation of V_O defects at the surface of the V_O -rich N- SnO_2 NS.

SnO_2 was determined the primary crystalline phase in the V_O -rich N- SnO_2 NS based on X-ray diffraction (XRD) patterns (Figure S4). The elemental composition was analyzed using energy-dispersive X-ray spectroscopy (EDX) mapping, showing N element's homogeneous distribution throughout the sample (**Figure 1d**). X-ray photoelectron survey spectrum (XPS) further revealed that Sn, O, and N elements are dominant (Figure S5). N 1s XPS spectra (**Figures 1e and S6**) showed a prominent characteristic signal appearing at 399.7 eV, assigned to the Sn-N bonds.^[16] Electron paramagnetic resonance (EPR) exhibited a signal at $g = 2.001$, which originated from the unpaired electrons trapped by V_O defect, further confirming the existence of V_O (**Figures 1f and S7**).^[17] The N_2 adsorption-desorption isotherm plots showed a mesoporous feature with a BET surface area of $101 \text{ m}^2 \text{ g}^{-1}$ (**Figures 1g and S8**).

The electrocatalytic CO_2RR performance of the V_O -rich N- SnO_2 NS was studied in a 0.1 M KHCO_3 solution. A control sample was prepared by annealing at a relative temperature of 350 °C under an identical flowing ammonia environment, which was found to contain a low content of V_O (denoted as V_O -poor N- SnO_2 NS). The pristine SnO_x NS and V_O -poor N- SnO_2 NS samples

were also well characterized by using a variety of techniques, including FESEM, TEM, XRD, XPS, and EPR (Figures S1-S2 and S4-S7). All the gaseous and liquid products during the CO₂RR were quantified by gas chromatography and nuclear magnetic resonance (¹H NMR). The *V_O*-rich N-SnO₂ NS generated a current density of 10 mA cm⁻² at a low potential of -0.97 V. In contrast, the *V_O*-poor N-SnO₂ (-1.04 V) and pristine SnO_x NS (>-1.20 V) required higher potentials to yield the same current density (**Figures 2a** and S9). For the *V_O*-rich N-SnO₂ NS, a prominent reductive peak observed at -0.2 V (**Figure 2a**) is due to the reduction of unstable oxide layers at the catalyst surface.^[18] The *V_O*-rich N-SnO₂ NS exhibited a high HCOO⁻ FE of 83% at a low potential of -0.9 V (**Figure 2b**). In contrast, only 68% and 70% HCOO⁻ FEs were determined on the pristine SnO_x NS and the *V_O*-poor N-SnO₂ NS, respectively, at the same potential. The superior HCOO⁻ selectivity of the *V_O*-rich N-SnO₂ NS can be attributed to the coexistence of N dopants and *V_O*. The partial current density for the HCOO⁻ production (*J_{HCOO}*⁻) reached 6.7 mA cm⁻² at -0.9 V on the *V_O*-rich N-SnO₂ NS catalyst, which is 1.5 and 2.9 times higher than the *V_O*-poor N-SnO₂ NS (4.6 mA cm⁻²) and the pristine SnO_x NS (2.3 mA cm⁻²) (**Figure 2c**), respectively. A high C1 product selectivity of >90% was on the *V_O*-rich N-SnO₂ NS catalyst at a potential range from -0.9 to -1.2 V (**Figure 2d**), revealing the pivotal effect of N dopants and *V_O* on enhancing CO₂RR performance. Notably, the outstanding CO₂RR activity to produce HCOO⁻ over the *V_O*-rich N-SnO₂ NS is record-high compared to the previously reported SnO_x-based catalysts (**Figure 2e** and Table S1). A Tafel slope of 120 mV dec⁻¹ was determined on the *V_O*-rich N-SnO₂ NS (**Figure 2f**), which is lower than those of the pristine SnO_x (168 mV dec⁻¹) and the *V_O*-rich N-SnO₂ (136 mV dec⁻¹), indicating that the first electron transfer is the rate-determining step for the CO₂RR.^[19] The electrochemical impedance spectroscopy (EIS) revealed that the charge-transfer resistance over the *V_O*-rich N-SnO₂ NS is smaller than both the *V_O*-poor N-SnO₂ NS and the pristine SnO_x NS (Figure S10). Also, the double-layer capacitance (*C_{dl}*) value of 12.1 mF cm⁻² of the *V_O*-rich N-SnO₂ NS was larger than 4.9 mF cm⁻² for pristine SnO_x (**Figures 2g** and S11), indicating an increased electrochemically active surface area (ECSA). Given a relatively low specific surface area of *V_O*-rich N-SnO₂ NS than pristine SnO_x

(**Figures 1g and S8**), the increased active site density is due to the richness of N dopants and V_O . A 10-hour potentiostat test maintained a stable current density at 8.0 mA cm^{-2} , confirming promising stability of the V_O -rich N-SnO₂ NS catalyst during the CO₂RR (**Figures 2h and S12**). NMR results further showed that the C1 product selectivity over the V_O -rich N-SnO₂ NS is greater than 89% after long-term CO₂RR electrolysis. In principle, the Sn⁴⁺ can be reduced to Sn⁰ during the CO₂RR process, which likely leads to a reduced HCOO⁻ selectivity.^[20] However, XPS measurement confirmed the stability of V_O -rich N-SnO₂ NS (**Figure S13**), without the formation of reduced Sn⁰ species after the 10-hour CO₂RR.

HAADF-STEM imaging was carried out to explore the local structure of Sn species on the V_O -rich N-SnO₂ NS (**Figure 3a**). The geometric phase analysis (GPA) for the HAADF image (**Figure 3b**) revealed an apparent local strain along the x -direction, attributed to V_O and N doping. The electron energy loss (EEL) map demonstrated uniform Sn element distribution (**Figure 3c**). EEL maps for O and N elements (**Figure 3d-3e**) confirmed the presence of V_O defect and N enrichment in the lattice-distorted regions (**Figure 3f**). The presence of N species over the pristine SnO_x NS can be excluded (**Figure S14**).

XAS spectroscopy analysis further can provide insights on the coordination information and electronic structures of the studied SnO_x catalysts. The spectral profiles of three samples aligned well with SnO₂ reference, and the oxidation state is +2, consistent with the estimation by the first-order derivative of spectra. The intensity of Sn K-edge X-ray absorption near-edge spectroscopy (XANES) over the V_O -rich N-SnO₂ NS was lower than others (inset of **Figure 3g**), likely due to less unoccupied electronic states in the presence of V_O and N dopant defects. The V_O -poor N-SnO₂ NS sample displayed a slightly higher peak intensity than the pristine SnO_x NS one, resulting from a high crystallinity degree of the V_O -poor N-SnO₂ NS.

Figure 3h-i presented the Sn K-edge extended X-ray fine structure spectroscopy (EXAFS) with a k^3 -weighted oscillation function. The local atomic structure's disordering can be determined following the amplitude oscillation sequence (**Figure 3h**). Both N-SnO₂ NS samples had almost identical oscillation amplitude, further supporting the argument above the relatively

low crystallinity for pristine SnO_x NS. **Figure 3i** displayed the Fourier transformed (FT) results of Sn K-edge k^3 -weighted EXAFS. The structural parameters of coordination numbers (CN), bond distances (R), and Debye-waller factors (σ^2) are summarized in Table S2. The nearest neighboring coordination was the first Sn-O bonding, followed by the first Sn-Sn shell and second Sn-O/Sn-Sn shells in the radial distance of about 3-4 Å. Despite V_O and N dopants' presence, no significant variation was observed on the interatomic distance (Sn-O), which can be attributed to O sites' replacement by N.^[21] The experimental analysis agrees with the theoretical computation, as shown in Figure S15. The N K-edge XAS results of the V_O -rich N- SnO_2 NS provided the foremost evidence for the presence of Sn-N bond/coordination (Figure S16), which was also consistent with DFT calculations (Figure S17).

Figure 3j showed the Sn M-edge spectra of these SnO_x NS samples. The signals and profiles for the V_O -poor N- SnO_2 NS and the V_O -rich N- SnO_2 NS were triplets and similar, with slightly variable intensities due to various concentrations of V_O defects and N dopants.^[22] For instance, the V_O -rich N- SnO_2 NS showed a higher absorption intensity than other control samples, reflecting the increase of Sn-N coordination and the decrease in the Sn-O coordination. Besides, the higher intensity at the pre-edge (486-487 eV) of the V_O -rich N- SnO_2 NS suggested a higher V_O concentration and dangling bonds at the surface^[23] relative to the V_O -poor N- SnO_2 NS. The O K-edge XANES of these samples were further analyzed (**Figure 3k**). The smaller signals (c, w, and z) on the V_O -rich N- SnO_2 NS were due to the transition probability to O 2p states. Hence, the Sn M-edge and O K-edge signals could provide evidence of electronic states trapped at V_O sites and unsaturated electrons at Sn sites.

Thiocyanate ion (SCN^-) was commonly used as an indicator to probing active metal sites, as it strongly adsorbs them.^[24] The measured current density for the V_O -rich N- SnO_2 NS with SCN^- adsorption was significantly decreased, indicating critical Sn active sites for the CO_2RR (**Figure 4a**). OH^- ions in electrolytes can play specific roles in the surrogate of $\text{CO}_2^{\bullet-}$. Thus, the anodic polarization curve was recorded in a 0.1 M N_2 -saturated KOH electrolyte to explore $\text{CO}_2^{\bullet-}$ adsorption on the V_O -rich N- SnO_2 NS catalyst surface. The sample exhibited a more negative

oxidation peak than V_O -poor N-SnO₂ NS and pristine SnO_x (**Figure 4b**).^[9]

Density functional theory (DFT) calculations were employed to understand the mechanism of HCOOH formation. Each of four surface oxygen atoms was replaced by a nitrogen atom on the N-doped SnO₂ surface. The most stable doping site is illuminated in Figure S18b. Our experiments have confirmed the existence of V_O at the SnO₂ surface, in agreement with the report by Batzill et al.^[25] The V_O defect was theoretically examined in this work, created at different oxygen sites to determine the lowest formation energy. The most preferred site was the oxygen vacancy close to the N dopant (Figure S18d). We compared the effects of the presence or absence of N dopants and V_O on CO₂RR activity for the HCOOH production. Four atomistic models were explicitly constructed, including pristine SnO₂ (SnO₂), N-doped SnO₂ (N-SnO₂), SnO₂ with V_O (V_O -SnO₂), and N-doped SnO₂ with V_O (V_O -N-SnO₂), as shown in Figure S18. The adsorption free energies of all possible intermediates in CO₂RR were calculated at the four surfaces (Table S3).

Meanwhile, the adsorption free energies of intermediates on transition metals (Rh, Pt, Pd, Cu, and Ag) were also calculated to accurately depict the scaling relations. The geometries and sites for all intermediates adsorbed on the V_O -N-SnO₂ and Pd are shown in Figure S19. Scaling relations^[26] in the adsorption free energies of intermediates were established using the $^*E_{COOH}$ as a descriptor. As shown in Figure S20, the adsorption free energies of all above transition metals and SnO₂ surfaces fit the same scaling relations well. We have established the correlation between the $^*E_{COOH}$ and reaction free energies to explore the thermodynamic trends of various elementary steps at different surfaces. Then, the potential-limiting step in HCOOH formation can be determined, in which the product selectivity can be predicted. As reported previously,^[27] two competitive reaction paths were found in the HCOOH formation, the HCOO* and COOH* paths, as illustrated in the following R1-R4 reactions. As the COOH* intermediate can be dissociated to CO* and OH*, the CO production is the primary side reaction *via* the COOH* path.

HCOO* path:





COOH* path:



As shown in **Figure 4c**, the solid and red lines represent the potential-limiting step for the CO₂RR to HCOOH. The more favorable pathway of HCOOH formation can be predicted from optimized limiting energies among the four elementary steps (R1-R4). The four elementary steps and their intersections generate two minimal reaction free energies at $^*E_{\text{COOH}}$ of 0.2 and 1.6 eV. Therefore, the HCOOH formation would follow two pathways involving four different elementary steps over different catalyst surfaces. Herein, the more negative the value of adsorption free energy, the stronger the bond strength of adsorbates to the surface. When the $^*E_{\text{COOH}}$ is lower than 0.7 eV, HCOOH production was most likely to follow the COOH* path, compared to the HCOO* path. Otherwise, the HCOO* path became preferable when the $^*E_{\text{COOH}}$ was larger than 0.7 eV. Therefore, the formation of HCOOH on SnO₂ based catalysts would follow the HCOO* path, as shown in **Figure 4c**.

The $^*E_{\text{COOH}}$ becomes weakened after N doping at SnO₂ surface (N-SnO₂), as the potential-limiting step's reaction free energy was lowered (**Figure 4c**). This variation indicates that the N doping in SnO₂ is the origin of improved HCOOH yields. Furthermore, in the presence of V_{O} , the $^*E_{\text{COOH}}$ is further weakened on the N-doped SnO₂ (V_{O} -N-SnO₂). The $^*E_{\text{COOH}}$ on the V_{O} -N-SnO₂ (-1.45 eV) is closer to the cross point (-1.60 eV), in which the HCOOH formation is optimal compared to other metal catalysts and pristine SnO₂. Thus, the N-doped SnO₂ with V_{O} is predicted with high HCOOH selectivity, consistent with our experiments. Besides, the H* absorption energy was 1.25 eV on the V_{O} -N-SnO₂, which was weaker than that on the N-SnO₂ (0.91 eV), V_{O} -SnO₂ (0.68 eV), and SnO₂ (0.60 eV) (**Figure 4d** and Table S3). Thus, the H* adsorption was restrained at the V_{O} -N-SnO₂ surface, capable of inhibiting the HER.

As the HCOOH formation proceeds via the HCOO* path, the HCOO* adsorption energy was used to distinguish the effects of V_{O} and N dopants. As the HCOO* adsorbed at the SnO₂ surface,

the O-2p orbitals interact with Sn-5p orbitals. The electronic structures could affect the strength of Sn-O bonds. Suppose a V_O formed at the SnO₂ surface (Figure 4e2). In that case, the local defect states' Fermi level leads to higher electronic energies for the interaction between Sn-5p and O-2p, resulting in weaker Sn-O bonds than that at the pristine SiO₂ surface (Figure 4e1). Furthermore, the weaker HCOO* adsorption in the vicinity of N dopants could be attributed to the unsaturated electronic states from N-2p orbitals (Figure 4e3). Therefore, for the N-doped SnO₂ with V_O (Figure 4e4), the local unsaturated O-2p and N-2p states result in higher energy than other models, consistent with calculated free energies in Table S3.

Encouraged by the exceptional CO₂RR performance, an integrated Zn-CO₂ battery with the V_O -rich N-SnO₂ NS cathode was assembled for CO₂-to-HCOO⁻ conversion during the discharging process while generating electricity. The charging process is via the well-studied oxygen evolution reaction (OER), i.e., an H₂O-to-O₂ conversion (Figures 5a and S21). A measured open-circuit voltage of the Zn-CO₂ battery (Figure 5b) was close to the theoretical value of 0.95 V.^[28] With the V_O -rich N-SnO₂ NS cathode, the Zn-CO₂ cell provided a charge-discharge potential gap of 1.47 V at 5.0 mA cm⁻². When the current density reached 10 mA cm⁻², the potential gap slightly increased to 1.66 V, demonstrating a good rechargeability (Figure 5b). Meanwhile, the Zn-CO₂ battery delivered a peak power density of 3.67 mW cm⁻² at 0.23 V, along with a large current density of 15.5 mA cm⁻² in the discharging mode (Figure 5c). Two combined Zn-CO₂ cells can power a yellow bulb with a voltage of 2.70 V (Figure 5d). At the first cycle, the Zn-CO₂ battery can be charged at 2.60 V and then exhibited a discharging voltage of 0.97 V, showing a narrow charge-discharge voltage gap of 1.63 V. After a continuous run of 33 h (100 cycles), the Zn-CO₂ battery exhibited a slightly decreased performance (Figure 5e). Furthermore, the Zn-CO₂ battery with V_O -rich N-SnO₂ NS cathode can efficiently generate HCOO⁻ with 41% FE at 2.0 mA cm⁻², which was gradually increased to 74% at 6.0 mA cm⁻² (Figure S22). Furthermore, powered by a commercial silicon solar cell, a CO₂RR-OER electrolyzer was designed by using V_O -rich N-SnO₂ NS cathode and a commercial Ir/C anode (Figure 5f). Under natural sunlight, the electrolyzer can successfully generate HCOO⁻ detected

using NMR analysis (Figure S23). Besides, under the simulated sunlight irradiation (**Figure 5g**), the CO₂RR-OER electrolyzer exhibited rapid and reproducible transient photocurrent responses, following by repeated ON/OFF illumination cycles. Powered by the simulated sunlight, a 10-hour test demonstrated a continuous generation of HCOO⁻ with an FE of ~55% (**Figure 5h**).

In summary, a 2D *V_O*-rich N-SnO₂ NS CO₂RR catalyst, featured with a thickness of ~10 nm and a high N-doping amount of 5 at.%, was synthesized by a facial ammonification treatment SnO_x NS from a hydrothermal process. The *V_O*-rich N-SnO₂ NS exhibited exceptional CO₂RR performance, generating a high HCOO⁻ FE of ~83% at a potential of -0.9 V and an FE of >90% for all C1 products at a wide potential range from -0.9 to -1.2 V. The improved CO₂RR activity and selectivity were originated from low coordinated Sn-N active sites with optimal electronic and geometric structures regulated by oxygen vacancy and nitrogen doping in SnO₂. Theoretical studies predicted that HCOO* protonation pathway becomes favorable due to the *V_O* and N dopants at the SnO₂ surface. The presence of N dopants and *V_O* also suppresses H* adsorption on SnO₂, inhibiting the HER process and enhancing HCOO⁻ FE. The innovative Zn-CO₂ battery and CO₂RR-OER electrolyzer by using the *V_O*-rich N-SnO₂ NS cathode demonstrated the great potential of directly converting CO₂ to HCOO⁻ through innovative electrochemical devices coupled with renewable energy sources such as solar energy.

Supporting Information

Supporting Information is available from the Wiley Online Library or the author.

Acknowledgments

Z.L. and A.C. contributed equally to this work. Y. Hou thanks the support of the National Natural Science Foundation of China (51702284, 21878270, 21922811, and 21961160742), Zhejiang Provincial Natural Science Foundation of China (LR19B060002), the Fundamental Research Funds for the Central Universities, and the Startup Foundation for Hundred-Talent Program of Zhejiang University. J. Xiao acknowledges the financial supports from the National Natural Science Foundation of China (91845103, 91945302 and 21802124), the fund supported by LiaoNing Revitalization Talents Program (XLYC1907099), and the Strategic Priority Research Program of Chinese Academy of Sciences (XDB36030200), and the Ministry of Science and Technology of China (2018YFA0704503). Q. Zheng acknowledges support by the

Hundred Talent Program of the Chinese Academy of Sciences. We thank BL10B endstataion of Hefei Lightsource for NEXAFS measurement. G. Wu acknowledges the support from National Science Foundation (CBET-1604392, 1804326).

Received: ((will be filled in by the editorial staff))

Revised: ((will be filled in by the editorial staff))

Published online: ((will be filled in by the editorial staff))

References

- [1] O. S. Bushuyev, P. De Luna, C. T. Dinh, L. Tao, G. Saur, J. van de Lagemaat, S. O. Kelley, E. H. Sargent, *Joule* **2018**, *2*, 825; W. Zheng, J. Yang, H. Chen, Y. Hou, Q. Wang, M. Gu, F. He, Y. Xia, Z. Xia, Z. Li, B. Yang, L. Lei, C. Yuan, Q. He, M. Qiu, X. Feng, *Adv. Funct. Mater.* **2020**, *30*, 1907658; T. Wang, Q. Zhao, Y. Fu, C. Lei, B. Yang, Z. Li, L. Lei, G. Wu, Y. Hou, *Small Methods* **2019**, *3*, 1900210; Y. Hou, M. Qiu, M. G. Kim, P. Liu, G. Nam, T. Zhang, X. Zhuang, B. Yang, J. Cho, M. Chen, C. Yuan, L. Lei, X. Feng, *Nat. Commun.* **2019**, *10*, 1392; N. Mohd Adli, W. Shan, S. Hwang, W. Samarakoon, S. Karakalos, Y. Li, D. A. Cullen, D. Su, Z. Feng, G. Wang, G. Wu, *Angew. Chem. Int. Ed.* **2020**, <https://doi.org/10.1002/anie.202012329>; Y. Li, H. Wang, C. Priest, S. Li, P. Xu, G. Wu, *Adv. Mater.* **2020**, 2000381.
- [2] M. Grasemann, G. Laurenczy, *Energy Environ. Sci.* **2012**, *5*, 8171; W. Zhou, K. Cheng, J. Kang, C. Zhou, V. Subramanian, Q. Zhang, Y. Wang, *Chem. Soc. Rev.* **2019**, *48*, 3193; Y. Zhu, X. Yang, C. Peng, C. Priest, Y. Mei, G. Wu, *Small* **2020**, 10.1002/sml.202005148.
- [3] S. Gao, X. Jiao, Z. Sun, W. Zhang, Y. Sun, C. Wang, Q. Hu, X. Zu, F. Yang, S. Yang, L. Liang, J. Wu, Y. Xie, *Angew. Chem. Int. Ed.* **2016**, *55*, 698; S. Gao, Y. Lin, X. Jiao, Y. Sun, Q. Luo, W. Zhang, D. Li, J. Yang, Y. Xie, *Nature* **2016**, *529*, 68; S. Gao, Z. Sun, W. Liu, X. Jiao, X. Zu, Q. Hu, Y. Sun, T. Yao, W. Zhang, S. Wei, Y. Xie, *Nat. Commun.* **2017**, *8*, 14503.
- [4] Y. Chen, M. W. Kanan, *J. Am. Chem. Soc.* **2012**, *134*, 1986; B. Kumar, V. Atla, J. P. Brian, S. Kumari, T. Q. Nguyen, M. Sunkara, J. M. Spurgeon, *Angew. Chem. Int. Ed.* **2017**, *56*, 3645; L. Fan, Z. Xia, M. Xu, Y. Lu, Z. Li, *Adv. Funct. Mater.* **2018**, *28*, 1706289.

- [5] A. Zhang, Y. Liang, H. Li, X. Zhao, Y. Chen, B. Zhang, W. Zhu, J. Zeng, *Nano Lett.* **2019**, *19*, 6547.
- [6] Y. Deng, Y. Huang, D. Ren, A. D. Handoko, Z. W. Seh, P. Hirunsit, B. S. Yeo, *ACS Appl. Mater. Interfaces* **2018**, *10*, 28572.
- [7] S. Zhang, P. Kang, S. Ubnoske, M. K. Brennaman, N. Song, R. L. House, J. T. Glass, T. J. Meyer, *J. Am. Chem. Soc.* **2014**, *136*, 7845.
- [8] N. Sreekanth, M. A. Nazrulla, T. V. Vineesh, K. Sailaja, K. L. Phani, *Chem. Commun.* **2015**, *51*, 16061.
- [9] J. Gu, F. Héroguel, J. Luterbacher, X. Hu, *Angew. Chem. Int. Ed.* **2018**, *57*, 2943.
- [10] Y. Hori, in *Modern Aspects of Electrochemistry*, (Eds: C. G. Vayenas, R. E. White, M. E. Gamboa-Aldeco), Springer New York, New York, NY 2008, 89.
- [11] S. Liu, J. Xiao, X. F. Lu, J. Wang, X. Wang, X. W. Lou, *Angew. Chem. Int. Ed.* **2019**, *58*, 8499; Y. Wei, J. Liu, F. Cheng, J. Chen, *J. Mater. Chem. A* **2019**, *7*, 19651; K. Wang, D. Liu, P. Deng, L. Liu, S. Lu, Z. Sun, Y. Ma, Y. Wang, M. Li, B. Y. Xia, C. Xiao, S. Ding, *Nano Energy* **2019**, *64*, 103954; Y. Zhu, J. Sokolowski, X. Song, Y. He, Y. Mei, G. Wu, *Adv. Energy Mater.* **2020**, *10*, 1902844; Q. Shi, S. Hwang, H. Yang, F. Ismail, D. Su, D. Higgins, G. Wu, *Mater. Today* **2020**, *37*, 93.
- [12] W. Ma, S. Xie, X. Zhang, F. Sun, J. Kang, Z. Jiang, Q. Zhang, D. Wu, Y. Wang, *Nat. Commun.* **2019**, *10*, 892; A. Zhang, R. He, H. Li, Y. Chen, T. Kong, K. Li, H. Ju, J. Zhu, W. Zhu, J. Zeng, *Angew. Chem. Int. Ed.* **2018**, *57*, 10954.

- [13] H. Li, J. Shang, H. Zhu, Z. Yang, Z. Ai, L. Zhang, *ACS Catal.* **2016**, *6*, 8276; D. Cui, L. Wang, K. Xu, L. Ren, L. Wang, Y. Yu, Y. Du, W. Hao, *J. Mater. Chem. A* **2018**, *6*, 2193; C. Mao, H. Cheng, H. Tian, H. Li, W. Xiao, H. Xu, J. Zhao, L. Zhang, *Appl. Catal., B.* **2018**, *228*, 87; Z. Jiang, W. Sun, W. Miao, Z. Yuan, G. Yang, F. Kong, T. Yan, J. Chen, B. Huang, C. An, G. A. Ozin, *Adv. Sci.* **2019**, *6*, 1900289.
- [14] Y. Wang, P. Han, X. Lv, L. Zhang, G. Zheng, *Joule* **2018**, *2*, 2551; Q. Wang, Y. Lei, D. Wang, Y. Li, *Energy Environ. Sci.* **2019**, *12*, 1730.
- [15] Y. Hou, M. R. Lohe, J. Zhang, S. Liu, X. Zhuang, X. Feng, *Energy Environ. Sci.* **2016**, *9*, 478.
- [16] X. Zu, X. Li, W. Liu, Y. Sun, J. Xu, T. Yao, W. Yan, S. Gao, C. Wang, S. Wei, Y. Xie, *Adv. Mater.* **2019**, *31*, 1808135.
- [17] Y. Xu, M. Zhou, C. Zhang, C. Wang, L. Liang, Y. Fang, M. Wu, L. Cheng, Y. Lei, *Nano Energy* **2017**, *38*, 304.
- [18] H. Li, N. Xiao, Y. Wang, C. Liu, S. Zhang, H. Zhang, J. Bai, J. Xiao, C. Li, Z. Guo, S. Zhao, J. Qiu, *J. Mater. Chem. A* **2020**, *8*, 1779.
- [19] X. Sun, L. Lu, Q. Zhu, C. Wu, D. Yang, C. Chen, B. Han, *Angew. Chem. Int. Ed.* **2018**, *57*, 2427.
- [20] N. Han, P. Ding, L. He, Y. Li, Y. Li, *Adv. Energy Mater.* **2020**, *10*, 1902338.
- [21] V. Briois, C. V. Santilli, S. H. Pulcinelli, G. E. S. Brito, *J. Non-Crystalline Solids* **1995**, *191*, 17.
- [22] S. O. Kucheyev, T. F. Baumann, P. A. Sterne, Y. Wang, T. van Buuren, A. V. Hamza, L. J.

Terminello, T. M. Willey, *Phys. Rev. B* **2005**, 72, 035404.

[23] P. M. Korusenko, S. N. Nesov, V. V. Bolotov, S. N. Povoroznyuk, A. I. Pushkarev, K. E. Ivlev, D. A. Smirnov, *Nucl. Instrum. Methods Phys. Res. B* **2017**, 394, 37; D. Wang, X. Li, J. Wang, J. Yang, D. Geng, R. Li, M. Cai, T. K. Sham, X. Sun, *J. Chem. Phys.* **2012**, 116, 22149; X. T. Zhou, J. G. Zhou, M. W. Murphy, J. Y. P. Ko, F. Heigl, T. Regier, R. I. R. Blyth, T. K. Sham, *J. Chem. Phys.* **2008**, 128, 144703.

[24] C. Lei, H. Chen, J. Cao, J. Yang, M. Qiu, Y. Xia, C. Yuan, B. Yang, Z. Li, X. Zhang, L. Lei, J. Abbott, Y. Zhong, X. Xia, G. Wu, Q. He, Y. Hou, *Adv. Energy Mater.* **2018**, 8, 1801912.

[25] M. Batzill, U. Diebold, *Prog. Surf. Sci.* **2005**, 79, 47.

[26] F. Abild-Pedersen, J. Greeley, F. Studt, J. Rossmeisl, T. R. Munter, P. G. Moses, E. Skúlason, T. Bligaard, J. K. Nørskov, *Phys. Rev. Lett.* **2007**, 99, 016105.

[27] J. T. Feaster, C. Shi, E. R. Cave, T. Hatsukade, D. N. Abram, K. P. Kuhl, C. Hahn, J. K. Nørskov, T. F. Jaramillo, *ACS Catal.* **2017**, 7, 4822; M. Zhang, Y. Wu, M. Dou, Y. Yu, *Catal. Lett.* **2018**, 148, 2935; K. Ye, A. Cao, J. Shao, G. Wang, R. Si, N. Ta, J. Xiao, G. Wang, *Sci. Bull.* **2020**, 65, 711.

[28] J. Xie, X. Wang, J. Lv, Y. Huang, M. Wu, Y. Wang, J. Yao, *Angew. Chem. Int. Ed.* **2018**, 57, 16996.

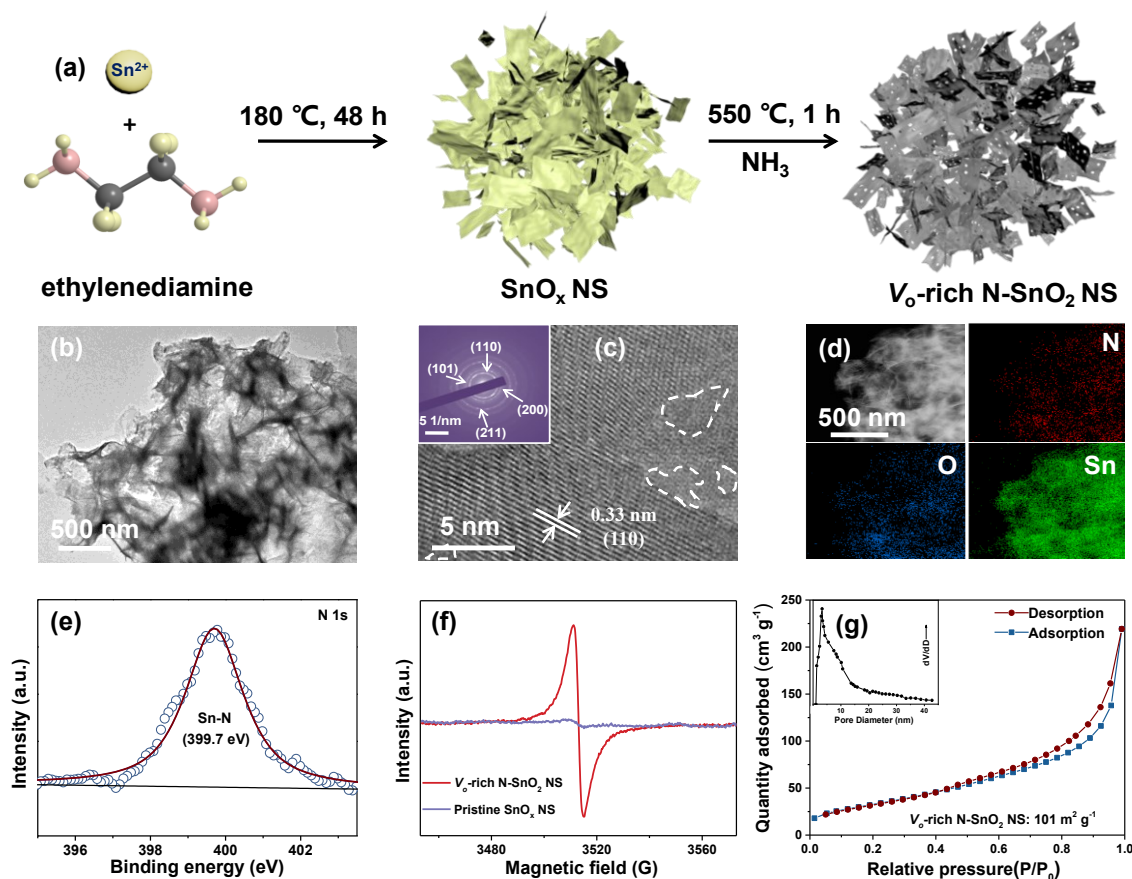


Figure 1. Structural characterization of the V_O -rich N-SnO₂ NS catalyst. (a) Schematic illustration of the synthetic procedure for the V_O -rich N-SnO₂ NS. (b-c) TEM and HR-TEM images of the V_O -rich N-SnO₂ NS, inset: corresponding SAED pattern, (d) EDX elemental mapping of N, O, and Sn elements in the V_O -rich N-SnO₂ NS, (e) high-resolution XPS N 1s spectroscopy for the V_O -rich N-SnO₂ NS, (f) EPR spectra of the pristine SnO_x NS and the V_O -rich N-SnO₂ NS, (g) N₂ adsorption-desorption isotherm curve of the V_O -rich N-SnO₂ NS, inset: corresponding pore size distribution.

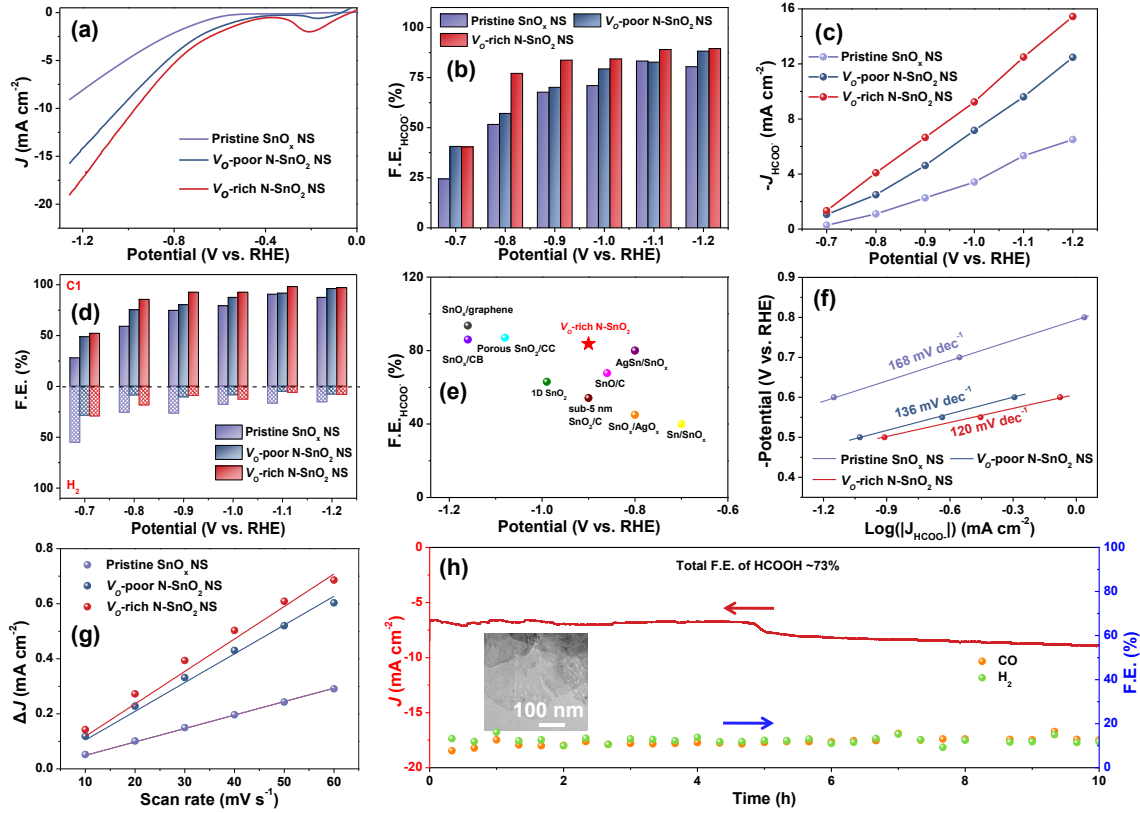


Figure 2. Electrochemical CO₂RR performance of the *V_O*-rich N-SnO₂ NS catalyst. (a) Polarization curves. (b) HCOO⁻ FE, (c) HCOO⁻ partial current densities. (d) FE for C₁ and H₂ products of the pristine SnO_x NS, the *V_O*-poor N-SnO₂ NS, and the *V_O*-rich N-SnO₂ NS catalysts in CO₂-saturated 0.1 M KHCO₃ electrolyte. (e) HCOO⁻ FE comparison among a series of SnO_x-based catalysts and the *V_O*-rich N-SnO₂ NS. (f) Tafel plots for the CO₂RR to HCOO⁻. (g) ECSAs of the pristine SnO_x NS, the *V_O*-poor N-SnO₂ NS, and the *V_O*-rich N-SnO₂ NS. (h) A 10-hour electrolysis test for the *V_O*-rich N-SnO₂ NS catalyst at -0.9 V, inset: TEM image of the *V_O*-rich N-SnO₂ NS after the electrolysis.

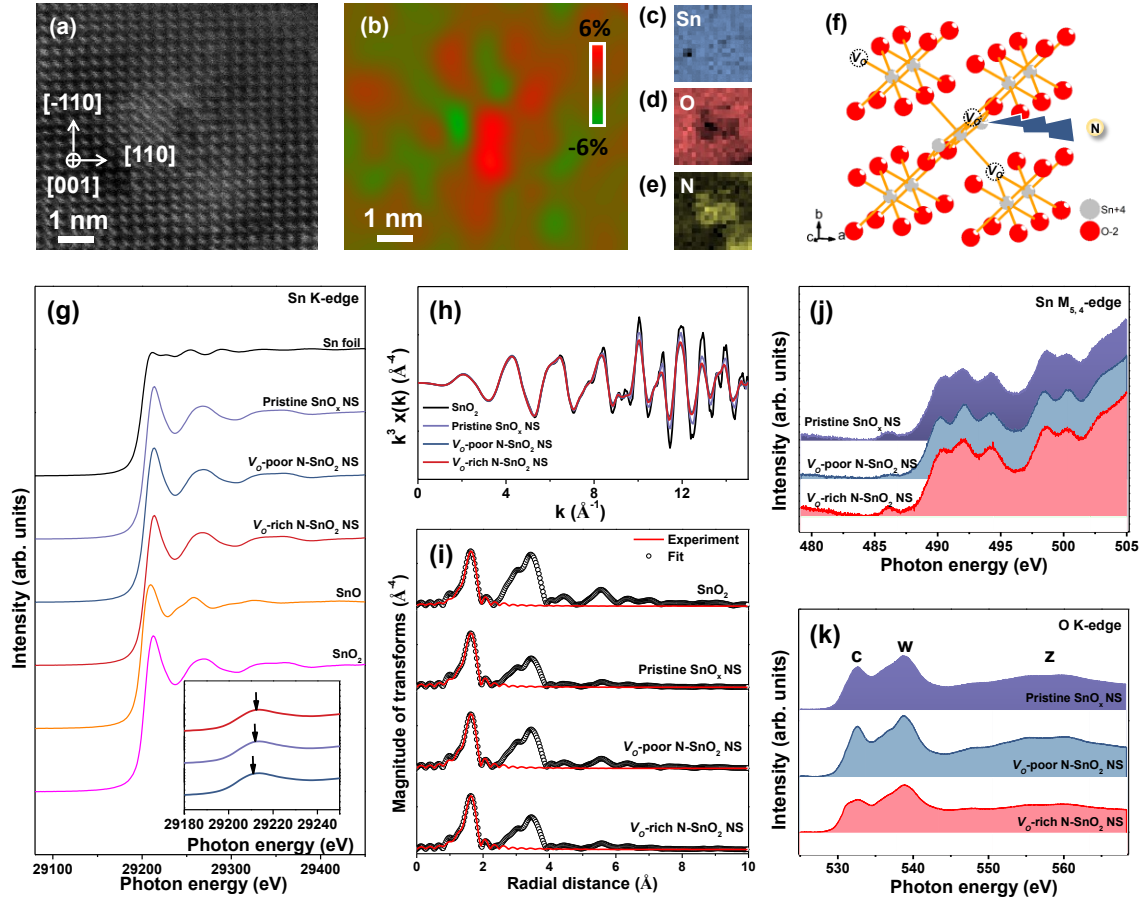


Figure 3. Fine structure of the V_O -rich N-SnO₂ NS. (a) A typical HAADF image along [001]. (b) Corresponding GPA analysis showed the lattice strain along the x -axis, induced by local V_O and doped N. EEL spectroscopy maps for the highlighted region in (b): (c) Sn, (d) O, and (e) N using Sn- $M_{4,5}$, O- K , and N- K edges of V_O -rich N-SnO₂ NS. (f) Illustration of N atom filling into V_O process. (g) Sn K-edge XANES spectra of the pristine SnO_x NS, the V_O -poor N-SnO₂ NS, and the V_O -rich N-SnO₂ NS comparing with standards of Sn foil, SnO, and SnO₂ (inset of Fig. 3g magnified view of edge positions). (h) Sn K-EXAFS oscillation functions $k^3\chi(k)$. (i) k^3 -weighted FT of EXAFS spectra for SnO₂, the pristine SnO_x NS, the V_O -poor N-SnO₂ NS, and the V_O -rich N-SnO₂ NS. (j) Sn $M_{5,4}$ -edge of XANES spectra and (k) O K-edge XANES spectra of the pristine SnO_x NS, the V_O -poor N-SnO₂ NS, and the V_O -rich N-SnO₂ NS.

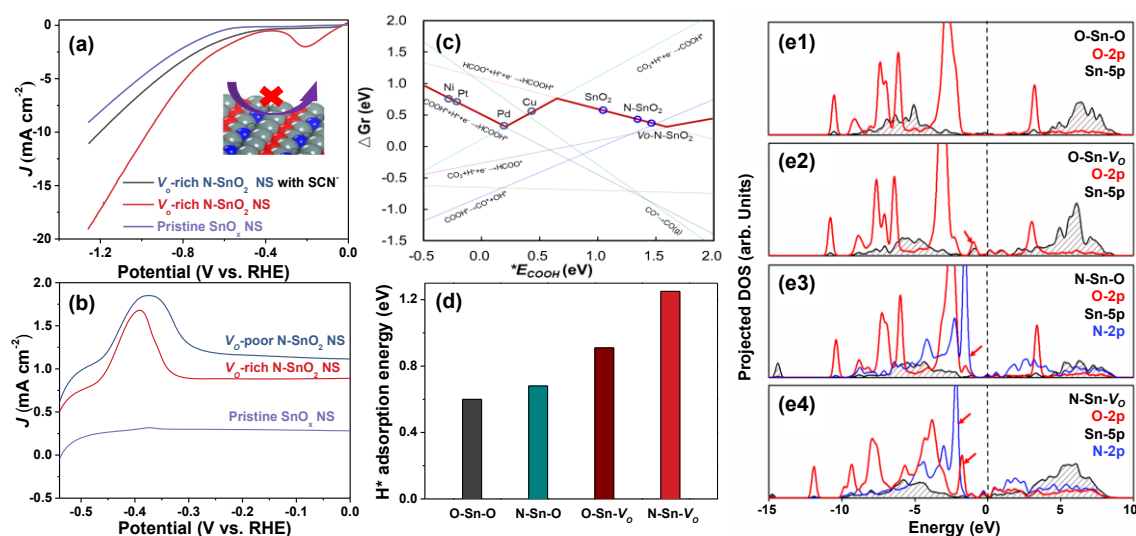


Figure 4. Understanding the active sites. (a) Poison experiments of the V_O -rich N-SnO₂ NS without and with KSCN adsorption under CO₂RR condition, inset: illustration of Sn-N bond impeded by SCN⁻ ions. (b) Single oxidative polarization curves in N₂-saturated 0.1 M KOH for the pristine SnO_x NS, the V_O -poor N-SnO₂ NS, and the V_O -rich N-SnO₂ NS. (c) Gibbs free reaction energy as a function of $*E_{\text{COOH}}$ on (211) surface of transition metals and (110) surface of tin-oxides at 298 K without potential correction. (d) H^{*} adsorption energy on O-Sn-O (SnO₂), N-Sn-O (N-SnO₂), O-Sn- V_O (V_O -SnO₂), and N-Sn- V_O (V_O -N-SnO₂). (e) Projected density of states of adsorbed HCOO* on (e1) the SnO₂ (110) facet, (e2) the SnO₂ (110) facet with an V_O , (e3) the SnO₂ (110) facet with the preferred site for N doping, (e4) N-doped SnO₂ (110) facet with an V_O , where red represents the O-2p states of HCOO*, black represents the Sn-5p states of SnO₂ (110) facet and blue stands for the N-2p states of N atom.

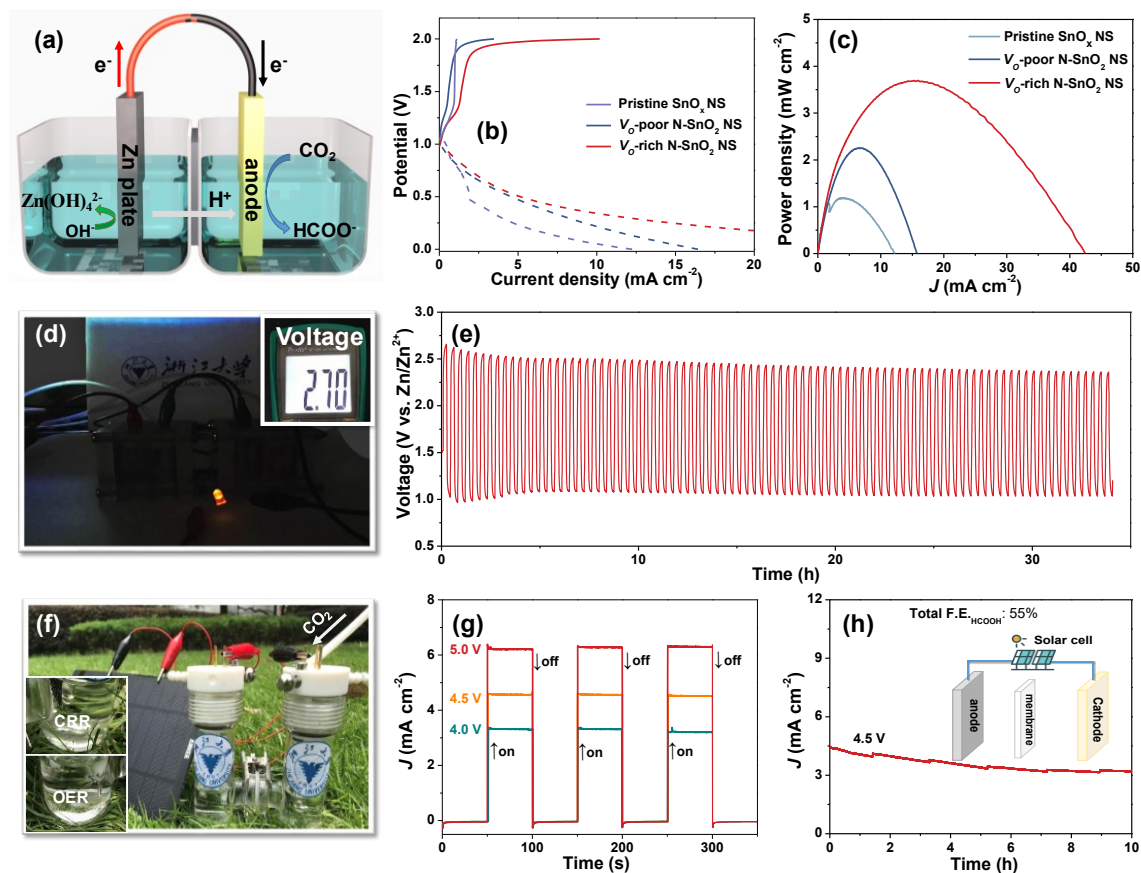
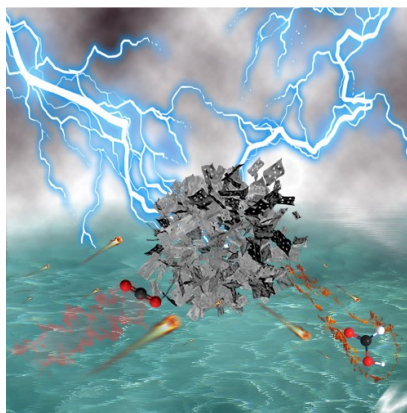


Figure 5. Zn-CO₂ battery by using the V_O-rich N-SnO₂ NS catalyst. (a) The model of Zn-CO₂ battery during discharging reaction. (b) Charging (solid line) and discharging (dotted line) curves. (c) Power density curves for the pristine SnO_x NS, the V_O-poor N-SnO₂ NS, and the V_O-rich N-SnO₂ NS. (d) A photograph to illuminate the lightening of a yellow bulb by using two Zn-CO₂ cells. (e) Galvanostatic discharge-charge cycling curve of the V_O-rich N-SnO₂ NS catalyst at 1.0 mA cm⁻², (f) photograph of CO₂RR-OER device driven by solar energy. (g) A CO₂RR-OER electrolyzer at different applied potentials powered by a solar panel under shredded simulated sunlight. (h) A chronoamperometric curve of CO₂RR-OER device powered by a solar panel at 4.5 V.

A novel V_O -rich N-doped SnO_2 nanosheet catalyst presents a possible synergistic effect of N dopants and oxygen vacancies. The catalyst exhibits exceptional catalyst activity and selectivity for the CO_2 eletroreduction to formate. Low coordination Sn-N moieties with optimal N dopants and O vacancies are identified as active sites with intrinsically enhanced activity. Theoretical calculations further elucidate the promotional role of dopants and vacancies at the SnO_2 surface concerning reaction pathways, adsorption of CO_2RR intermediates, and reaction energies of HCOO^* protonation.



Keyword: Dopants; vacancies; CO_2 electroreduction; formate; Zn- CO_2 batteries

Zhongjian Li, Ang Cao, Qiang Zheng, Yuanyuan Fu, Tingting Wang, K. Thanigal Arul, Jeng-Lung Chen, Bin Yang, Nadia Mohd Adli, Lecheng Lei, Chung-Li Dong, Jianping Xiao,* Gang Wu,* Yang Hou*

Elucidation of the Synergistic Effect of Dopants and Vacancies on Promoted Selectivity for CO_2 Electroreduction to Formate